Supplement of Atmos. Meas. Tech., 16, 3653–3678, 2023
https://doi.org/10.5194/amt-16-3653-2023-supplement


Atmospheric Measurement Techniques
Open Access
EGU

*Supplement of*

# Concept, absolute calibration, and validation of a new benchtop laser imaging polar nephelometer

**Alireza Moallemi et al.**

*Correspondence to:* Martin Gysel-Beer (martin.gysel@psi.ch)

**Supplementary Section S1:**

**Supplementary tables:**

**Table S1. size specification of the PSL samples. A material density of 1050 kg $m^{-3}$ for PSL was used for diameter conversion.**

| Certified geometric mean diameter (nm) | Specified coefficient of variation | AAC Aerodynamic diameter set point (nm) | Volume equivalent diameter ($D_{ve}$) of AAC aerodynamic diameter set point (nm) |
|---|---|---|---|
| 600 ± 9 | 1.7% | 620 | 603 |
| 240 ± 5 | 1.5% | 250 | 242 |

**Table S2. AAC aerodynamic diameter set point and corresponding equivalent volume diameter for tested DEHS aerosols. A material density of 900 kg $m^{-3}$ for DEHS was used for diameter conversion.**

| AAC aerodynamic diameter set point (nm) | $D_{ve}$ (nm) |
|---|---|
| 200 | 215 |
| 250 | 267 |
| 400 | 425 |
| 600 | 636 |
| 800 | 847 |

**Table S3. Parameters of the experiments performed with AAC selected mono-disperse DEHS aerosol samples: AAC set point (aerodynamic diameter), corresponding $D_{ve}$ (converted using material density of 900 kg m$^{-3}$ and assuming spherical shape), particle number concentration measured by the CPC ($N_{cpc}$). The following columns present size distribution parameters retrieved from phase functions measured by the uNeph using the least square minimization scheme: geometric mean diameter ($D_{ret}$), geometric standard deviation ($GSD_{ret}$), and particle number concentration ($N_{ret}$). The last two columns present the relative deviation of retrieved parameters from corresponding independently determined values.**

| AAC set point | AAC $D_{ve}$ | $N_{CPC}$ mean±SD | $D_{ret}$ | $GSD_{ret}$ | $N_{ret}$ | $(D_{ve} - D_{ret}) / D_{ve}$ | $(N_{CPC} - N_{ret}) / N_{CPC}$ |
|---|---|---|---|---|---|---|---|
| (nm) | (nm) | (cm$^{-3}$) | (nm) | (-) | (cm$^{-3}$) | (%) | (%) |
| 200 | 215 | 189.5 ± 8 | 214 | 1.035 | 185.7 | -0.5% | +2.0% |
| 400 | 425 | 494.3 ± 11 | 413 | 1.065 | 514 | -2.8% | -4.0% |
| 600 | 636 | 58.8 ± 4 | 612 | 1.05 | 61.8 | -3.8% | -5.0% |
| 800 | 847 | 70.2 + 5 | 817 | 1.06 | 73.7 | -3.5% | -6.0% |

**Supplementary figures:**

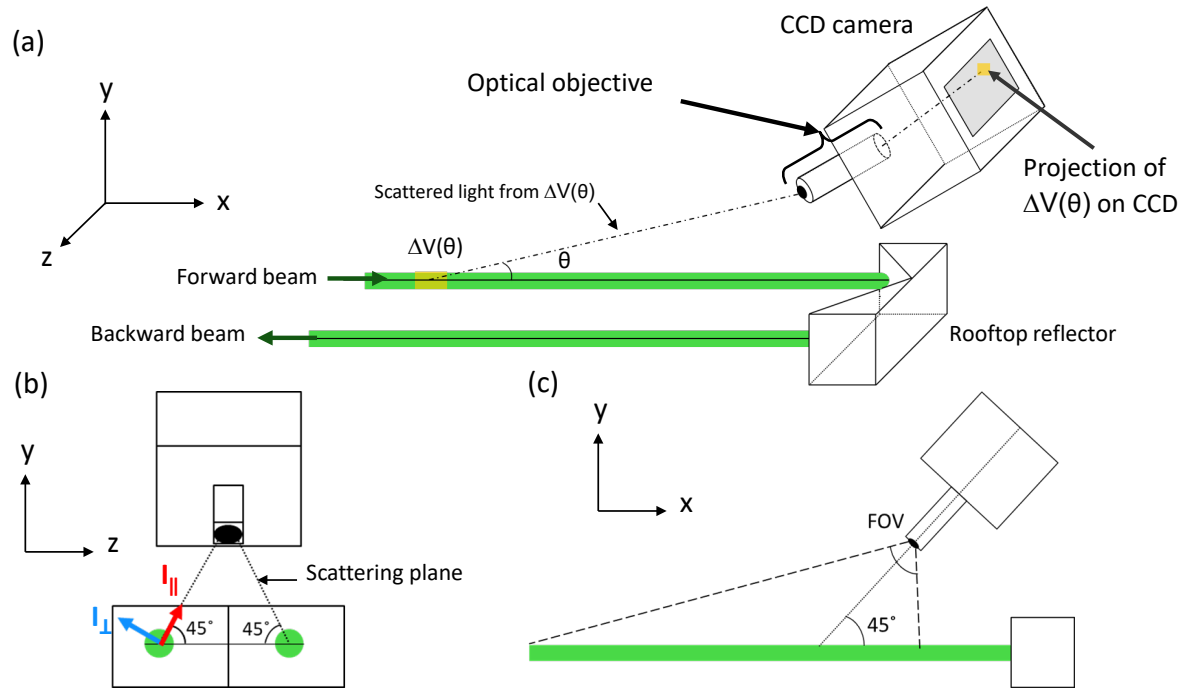


**Figure S1. Scattering geometry in the uNeph**

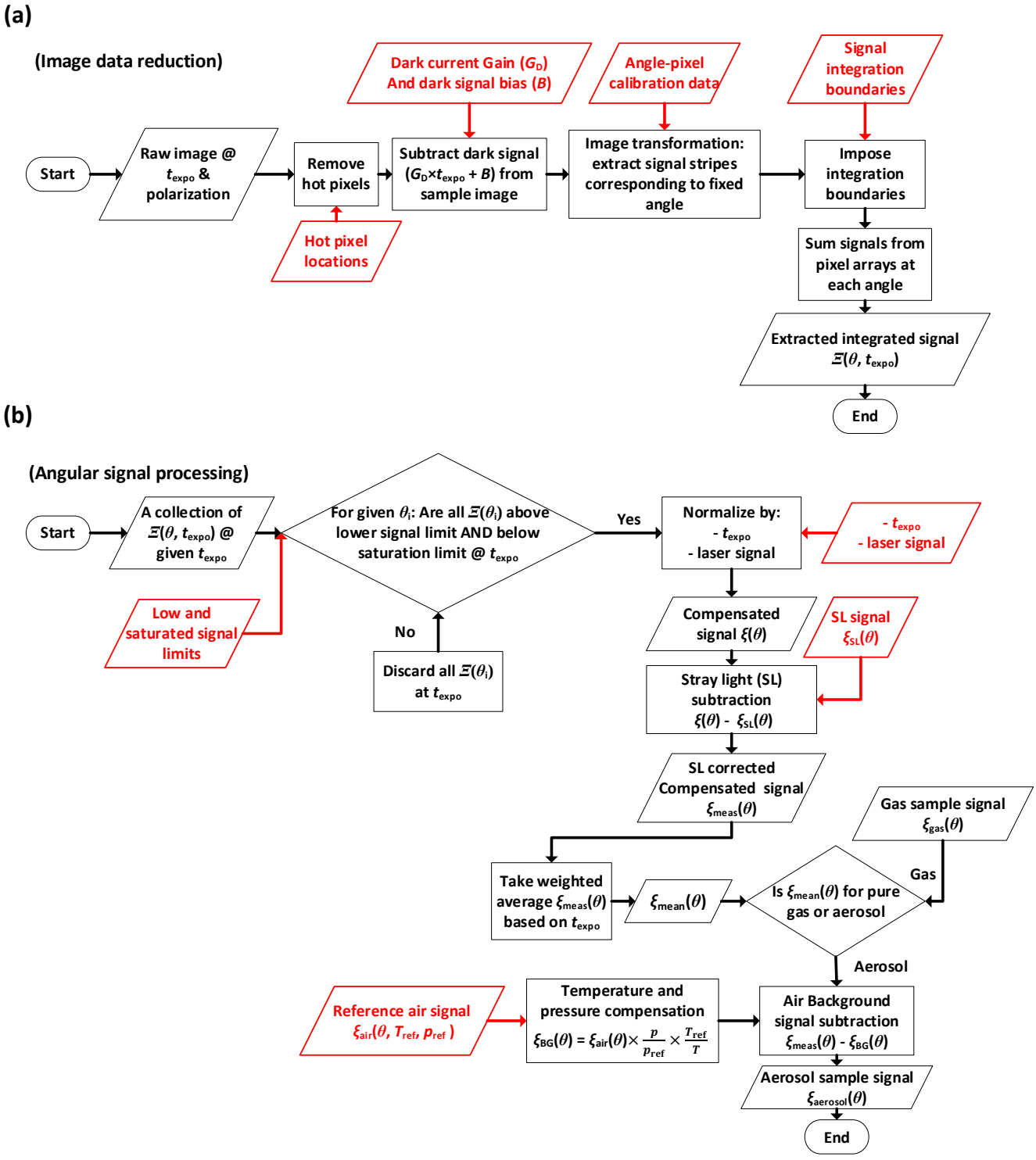


**Figure S2. Flowchart of all the data processing steps. Red color indicates calibration or auxiliary data.**

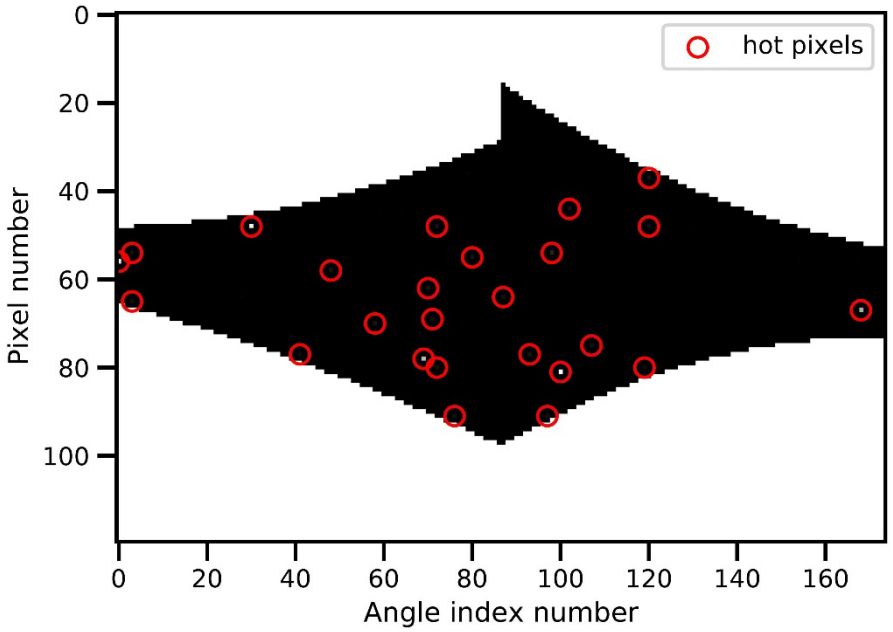


**Figure S3. Dark image in angle-pixel coordinate with hot pixels specified. To better visualize the hot pixels, the dark image shown corresponds to a dark image obtained with exposure time of 900 s.**

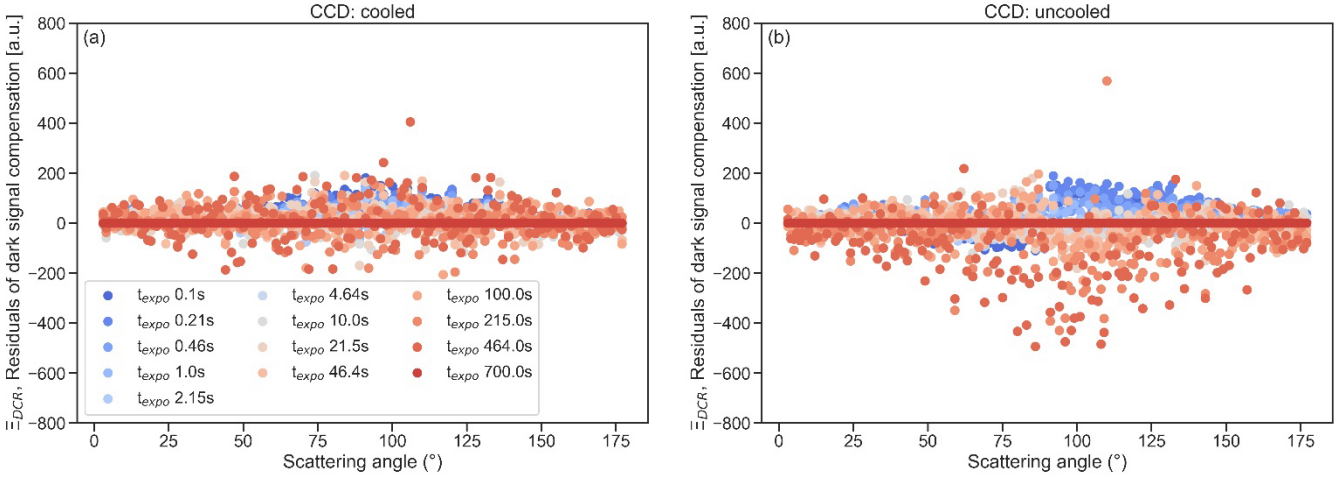


**Figure S4. Residual signal from dark signal correction on the data for the cooled (Panel a) and uncooled CCD (Panel b). The constants $G_{DS}(\theta)$ and $\Xi_{PB}(\theta)$ were not perfectly optimized for the backward angle range (90°-180°) in the uncooled case leaving some systematic exposure time dependence in the residuals. Nevertheless, the residuals of ~200 a.u. or less for exposure times shorter than 215 s are sufficiently small given that the upper limit of valid signals (saturation) occurs at around $2 \cdot 10^5$ to $2 \cdot 10^6$ a.u. (Fig. S12).**

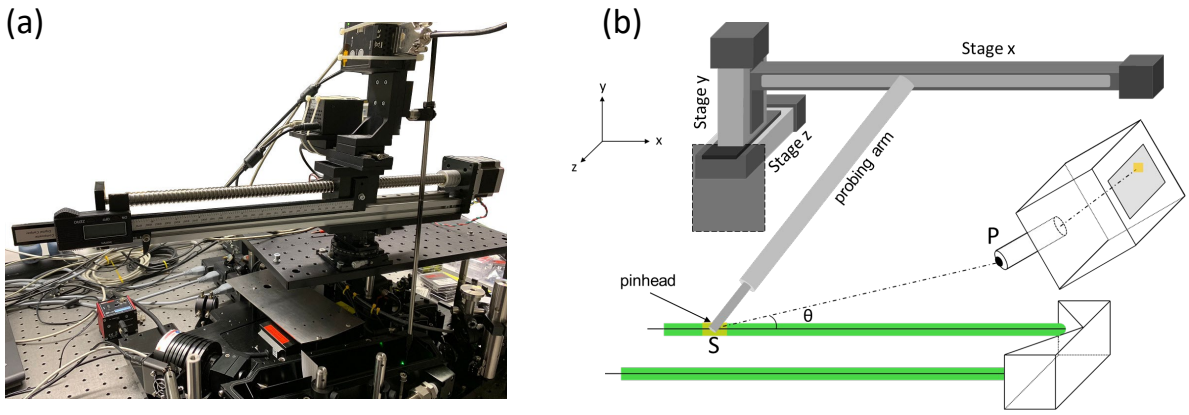


**Figure S5. (a) A picture of the 3D positional probe mounted on top the uNeph. (b) a 3D scheme of the positional probe, probing an example point S along the laser beam of the uNeph.**

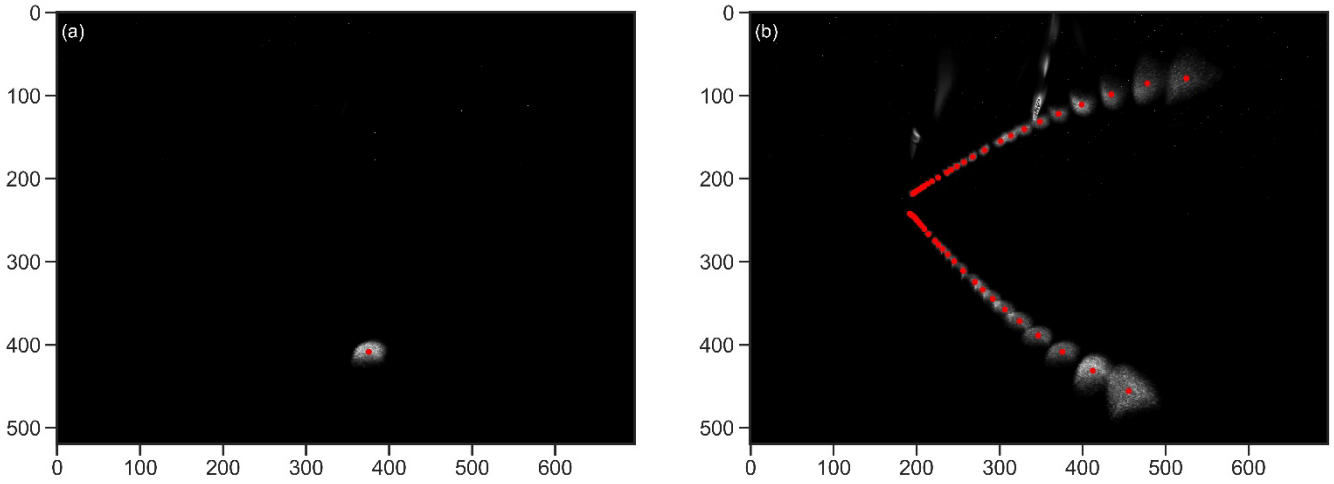


**Figure S6. (a) An example of angular calibration image data at a point corresponding to the scattering angle of approximately 68°. (b) a composite image of all calibration data. The red dots in the images corresponds to the pixel of the centre of mass of the given spots with is considered as the pixel corresponding to the location of the 3D positional probe's pinhead. It should be noted that the spots closer to the detection units appear larger while the spots further from the detection unit appear smaller.**

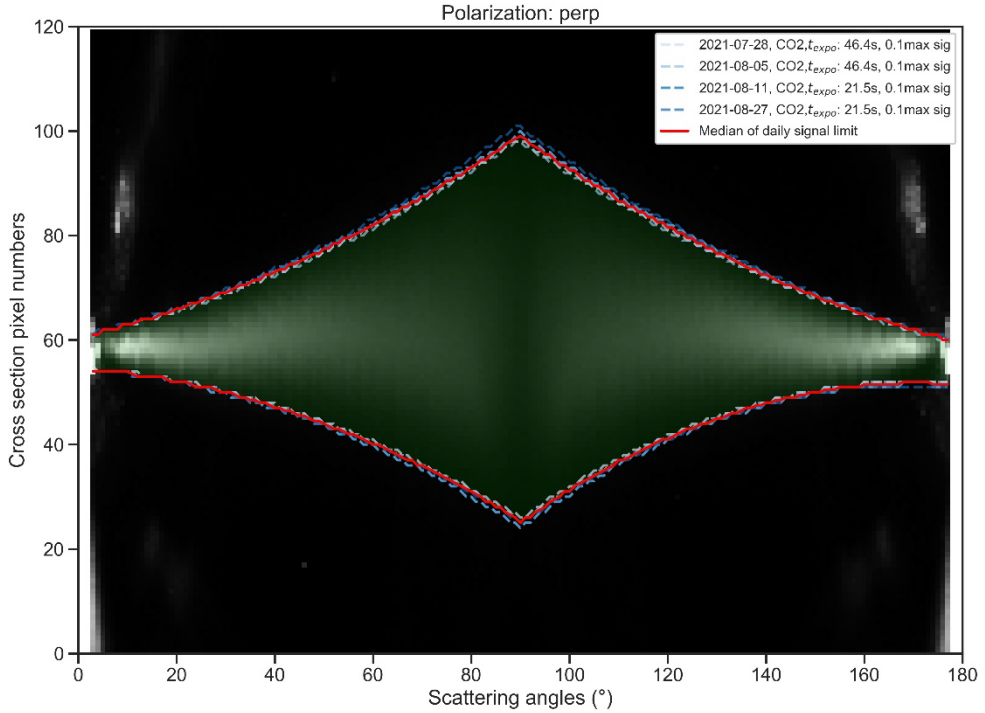


**Figure S7. The signal integration limits over scattering angles obteianed from the $CO_2$ measurements collected in different days.**

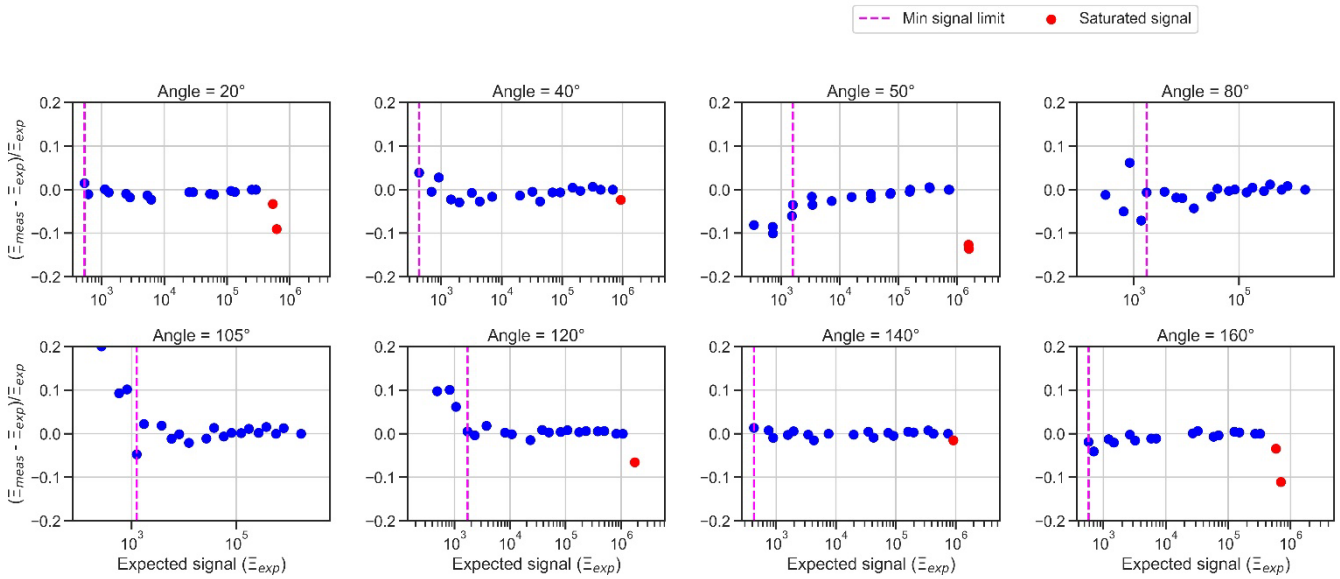


**Figure S8. Relative error vs $\Xi_{exp}$ for particle free air sample signals over different scattering angles for both polarization states and for a cooled CCD condition.**

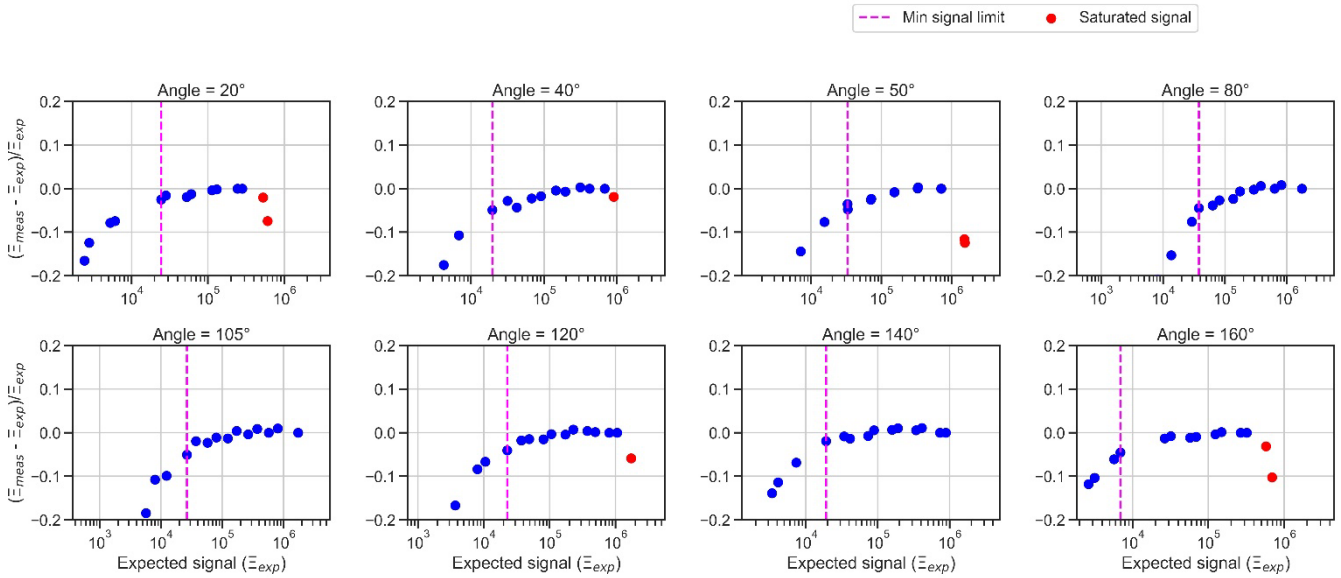


**Figure S9. Relative error vs $\Xi_{exp}$ for particle free air sample signals over different scattering angles for both polarization states and for an uncooled CCD condition.**

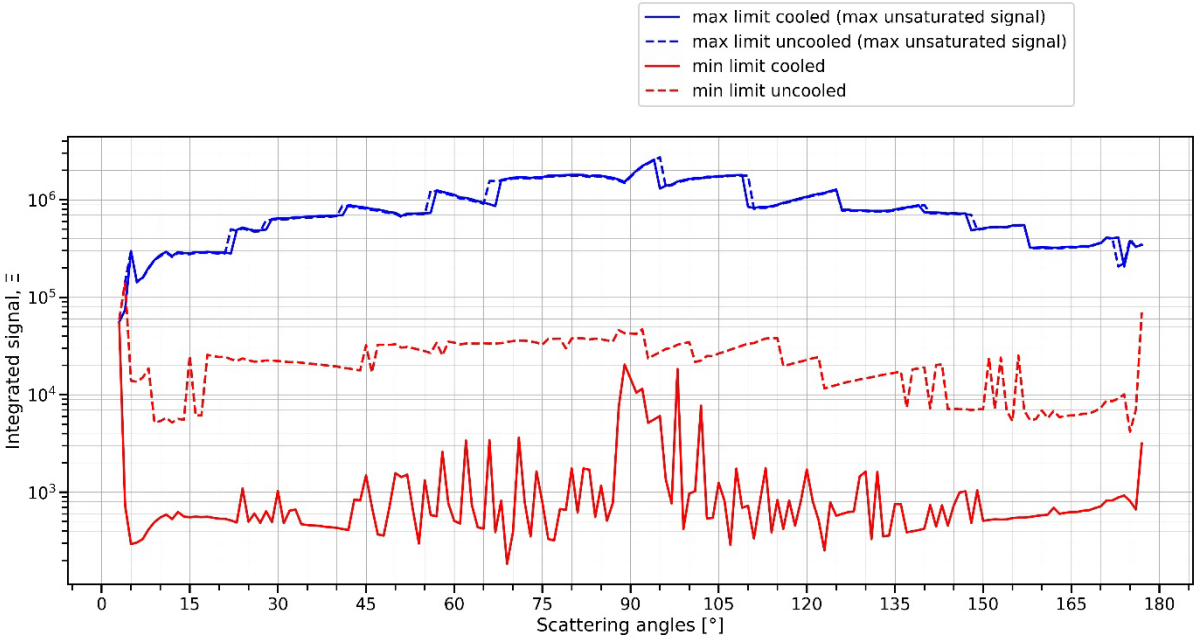


**Figure S10. Lower and upper limits for valid signal for cooled (solid line) and uncooled (dashed lines) CCD cases based on air measurements taken over a broad range of $t_{expo}$. The upper limit is the signal above which at least one saturated pixel exists and the lower limit is the lowest signal below which the relative difference between $\Xi_{exp}$ and $\Xi_{meas}$ increases above 6%.**

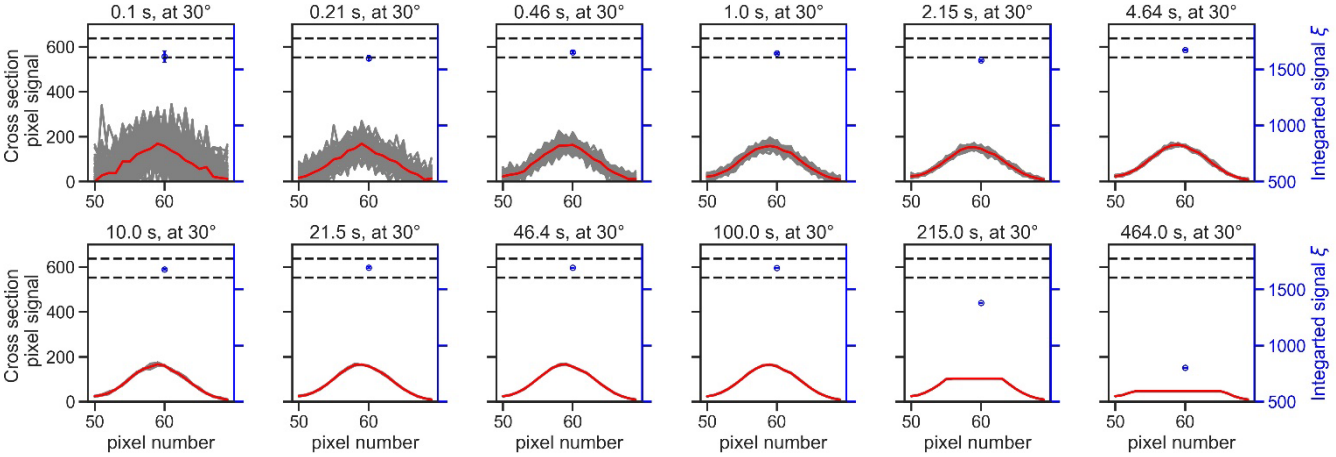


**Figure S11. Cross section signal (normalized by $t_{expo}$ and laser power signal) and integrated signal (normalized by $t_{expo}$ and laser power signal) behaviour over a range of exposure times (see plot titles) for filtered air samples at a scattering angle of 30°. Samples taken at polarization state 2. The mean integrated signal, $\xi$, with corresponding standard error of the mean as error bars in blue, plotted against right ordinate scale. The horizontal dashed line indicates ±5% variation around the mean $\xi$ at $t_{expo}$ = 100 s.**

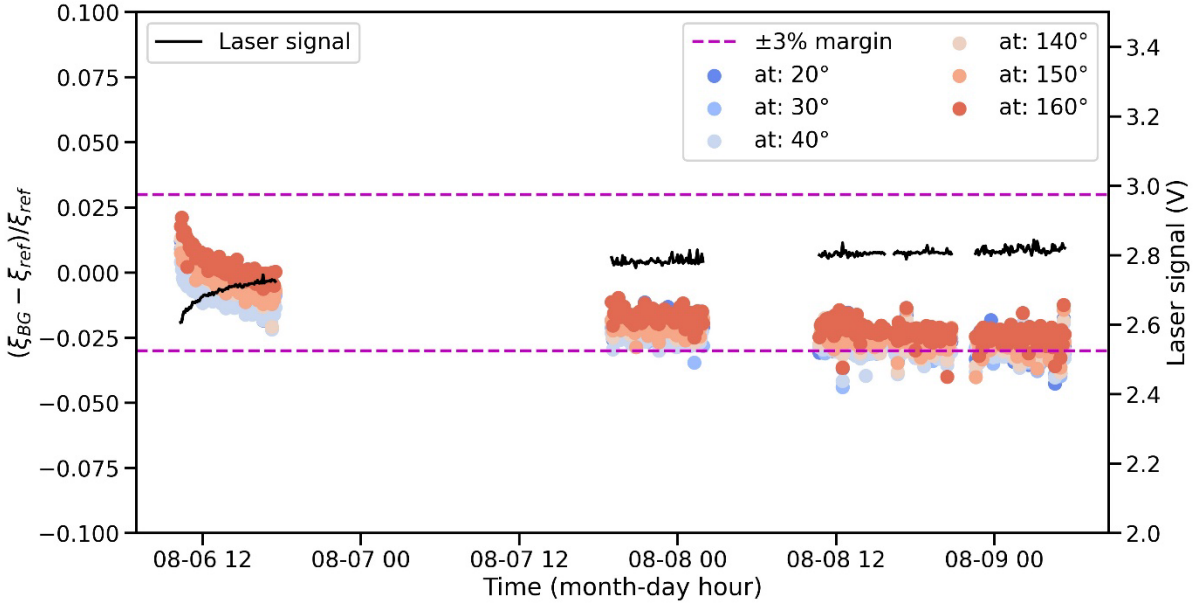


**Figure S12. Relative difference of air background ($\xi_{BG}$) to an arbitrary air reference point ($\xi_{ref}$, sample taken on the 2021-08-10 17:43 - 17:47) during a multiday measurement. This is shown for measurements of polarization state 1 at different scattering angles (5 min averages). The horizontal dashed lines indicate ±3% around the arbitrarily chosen reference point $\xi_{ref}$.**

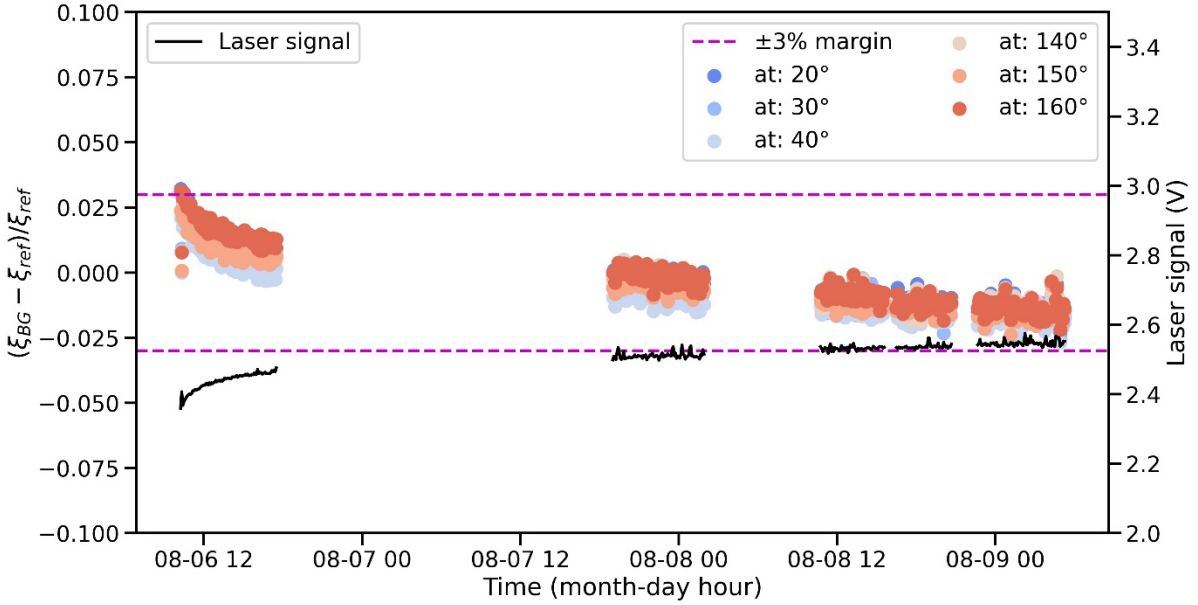


**Figure S13. Same as Fig. S12 for presenting polarization state 2 results with the arbitrary air reference point taken on the 2021-08-10 18:21 - 18:26).**

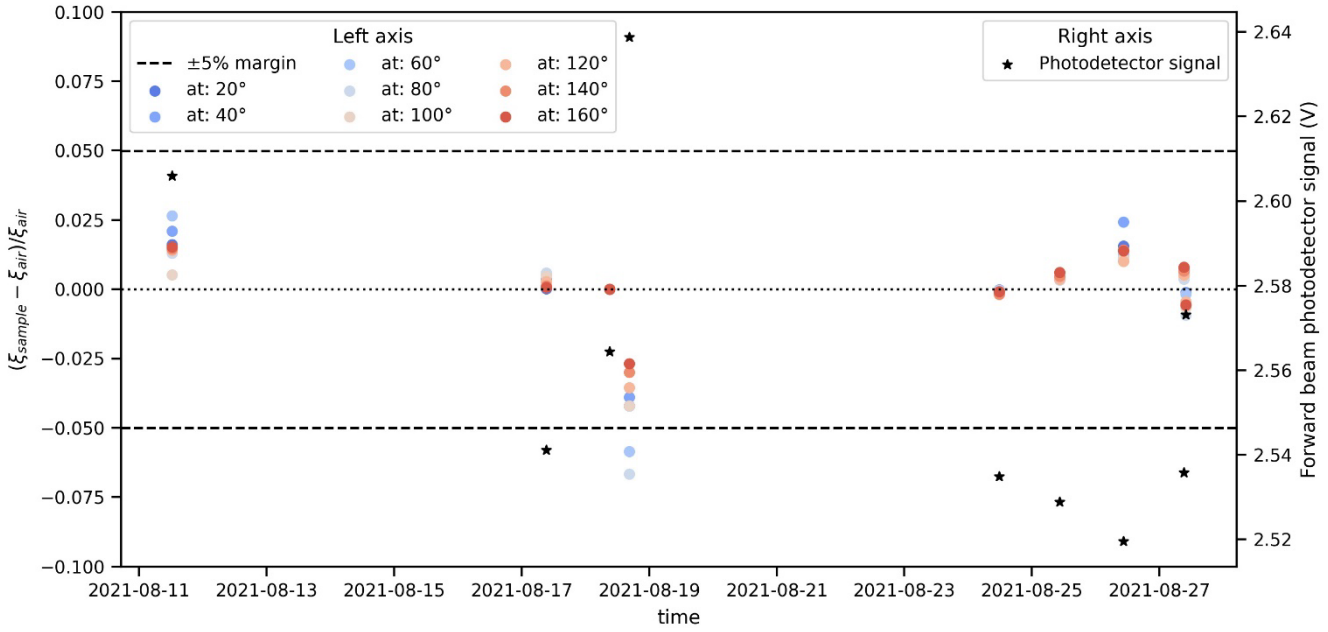


**Figure S14. Day to day particle-free air signal variability. The reference air signal assumed to calculate the relative difference was the sample taken on 2021-08-18.**

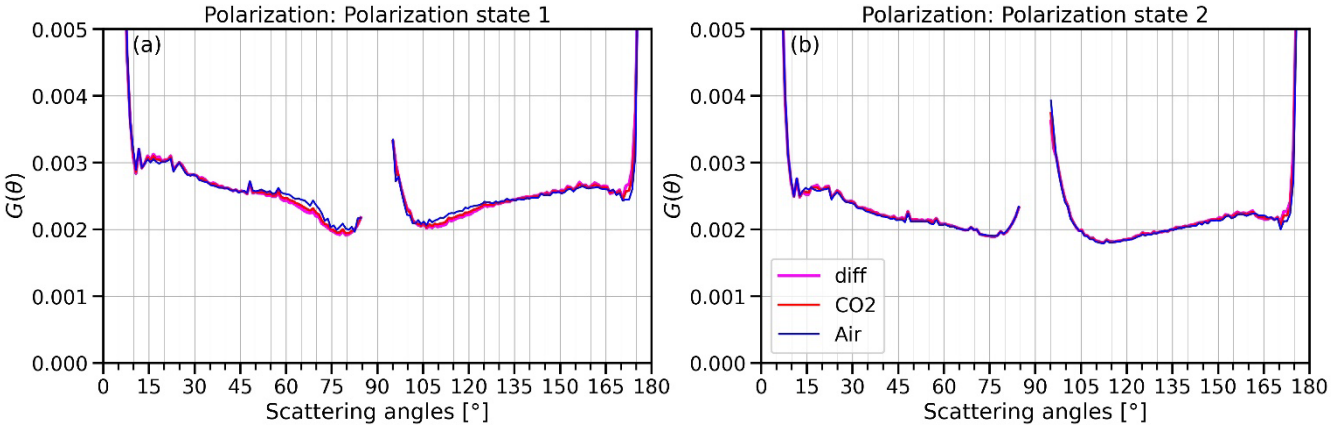


**Figure S15. (a) and (b) respectively shows $G_1(\theta)$ and $G_2(\theta)$ values derived from difference in $CO_2$ and air measurements (diff) and from individual gas ($CO_2$ and air) measurements.**

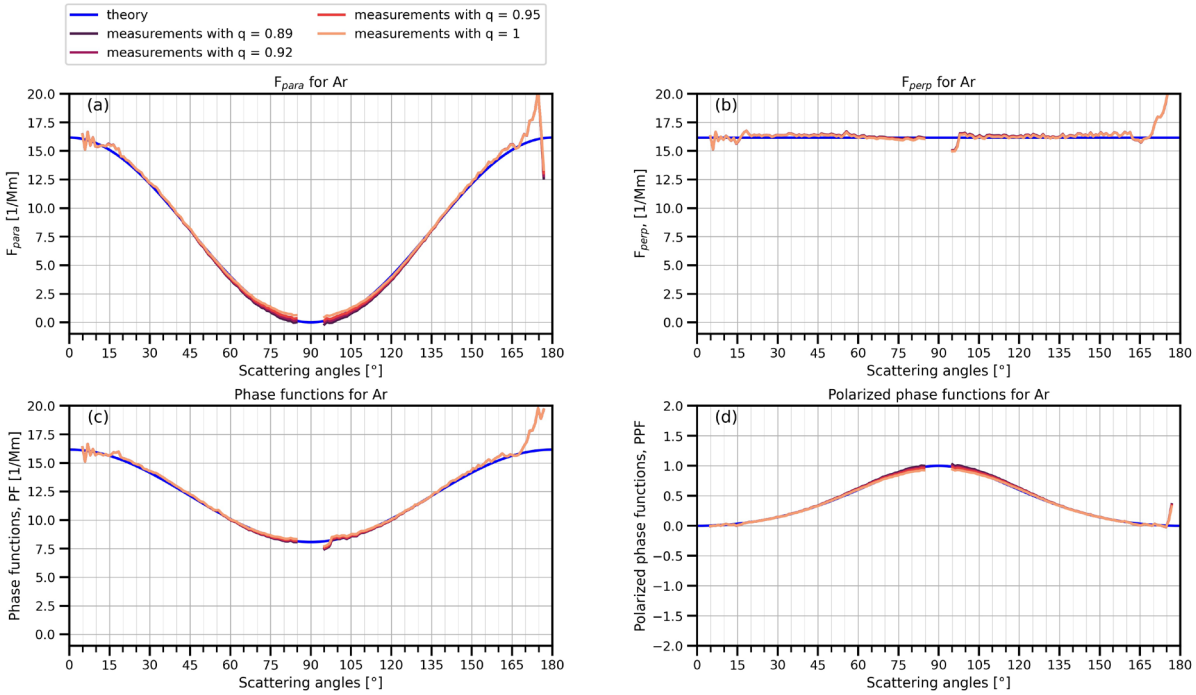


**Figure S16. (a) parallel phase function, $F_{para}$, (b) perpenicular phase function, $F_{perp}$, (c) phase function $F_{11}$, and (d) polarized phase function, $-F_{11}/F_{12}$, for uNeph measurements of Ar gas, given different $q$ value assumptions. The blue line corresponds to the theoretical angular light scattering of Ar based on Rayleigh scattering.**

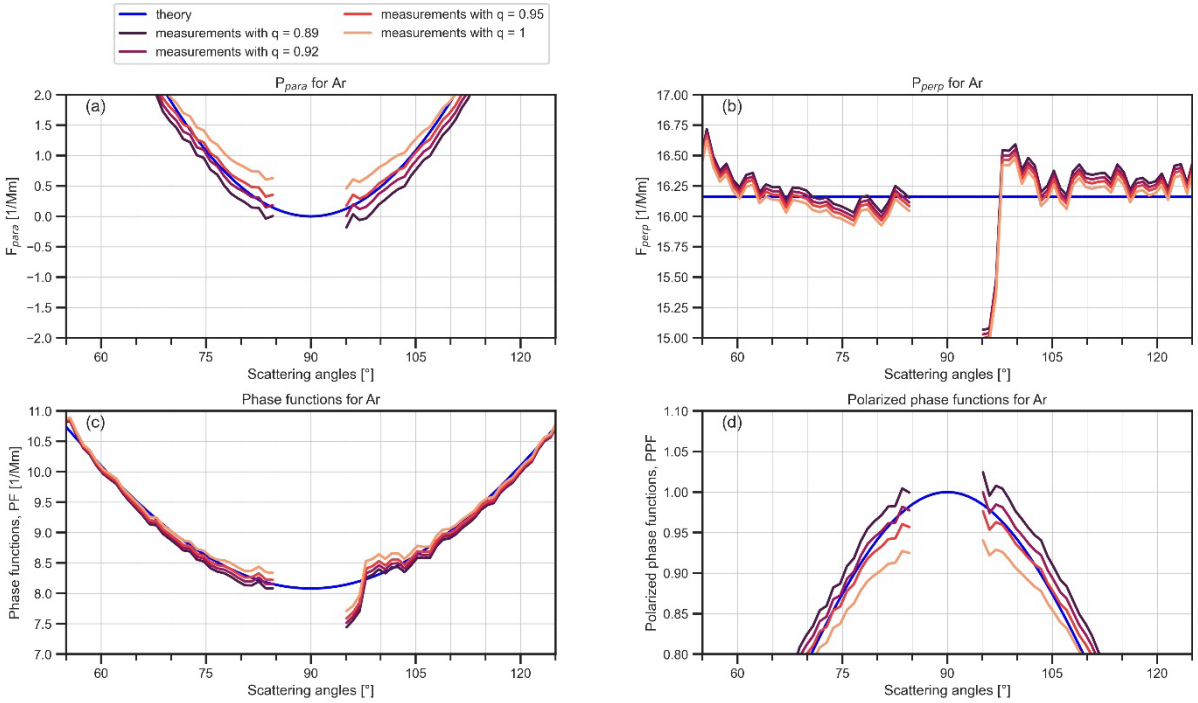


**Figure S17. Same as Fig. S16 but for zooming in to angle range from 55° to 125°. We selected $|q_i| = 0.92$ and $|q_i| = 0.95$ as appropriate values for forward and backward beams, respectively.**

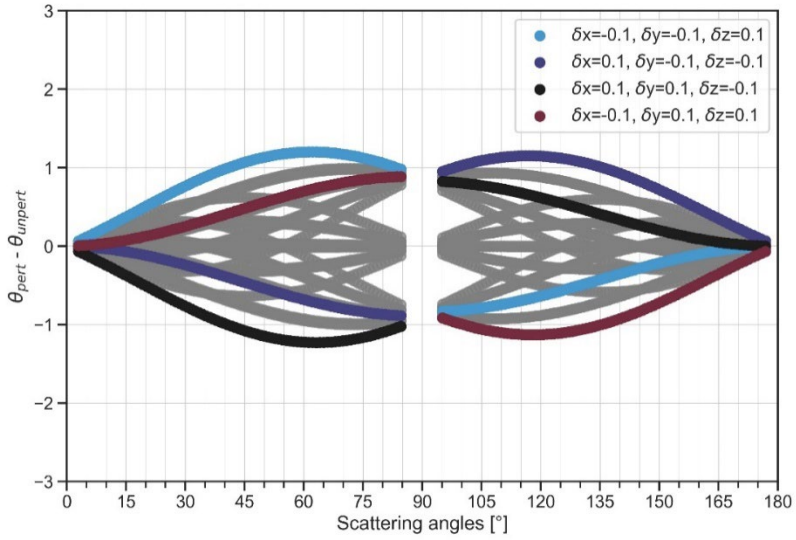


**Figure S18. Angle difference between perturbed and unperturbed case. The unperturbed case is based on the best pinhole estimate.**

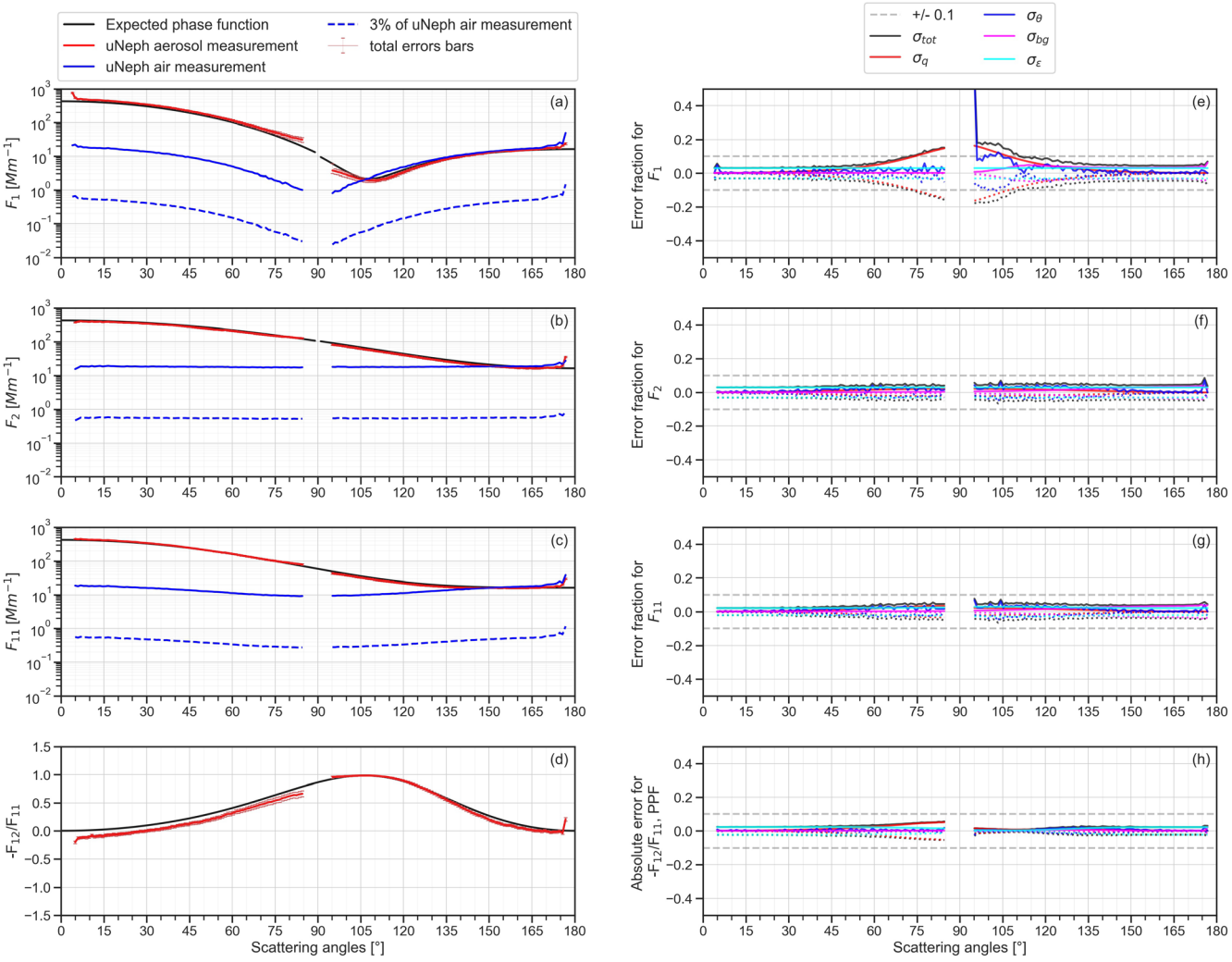


**Figure S19. (a, b, c, d) angular light scattering measurements with total errors for 250 nm (AAC aerodynamic set point) DEHS aerosol particles at high concentration (3010 #/cc). (e, f, g,) relative contributions of considered error factors for $F_1$, $F_2$, and $F_{11}$. (h) Absolute contributions of considered error factors for $-F_{12}/F_{11}$**

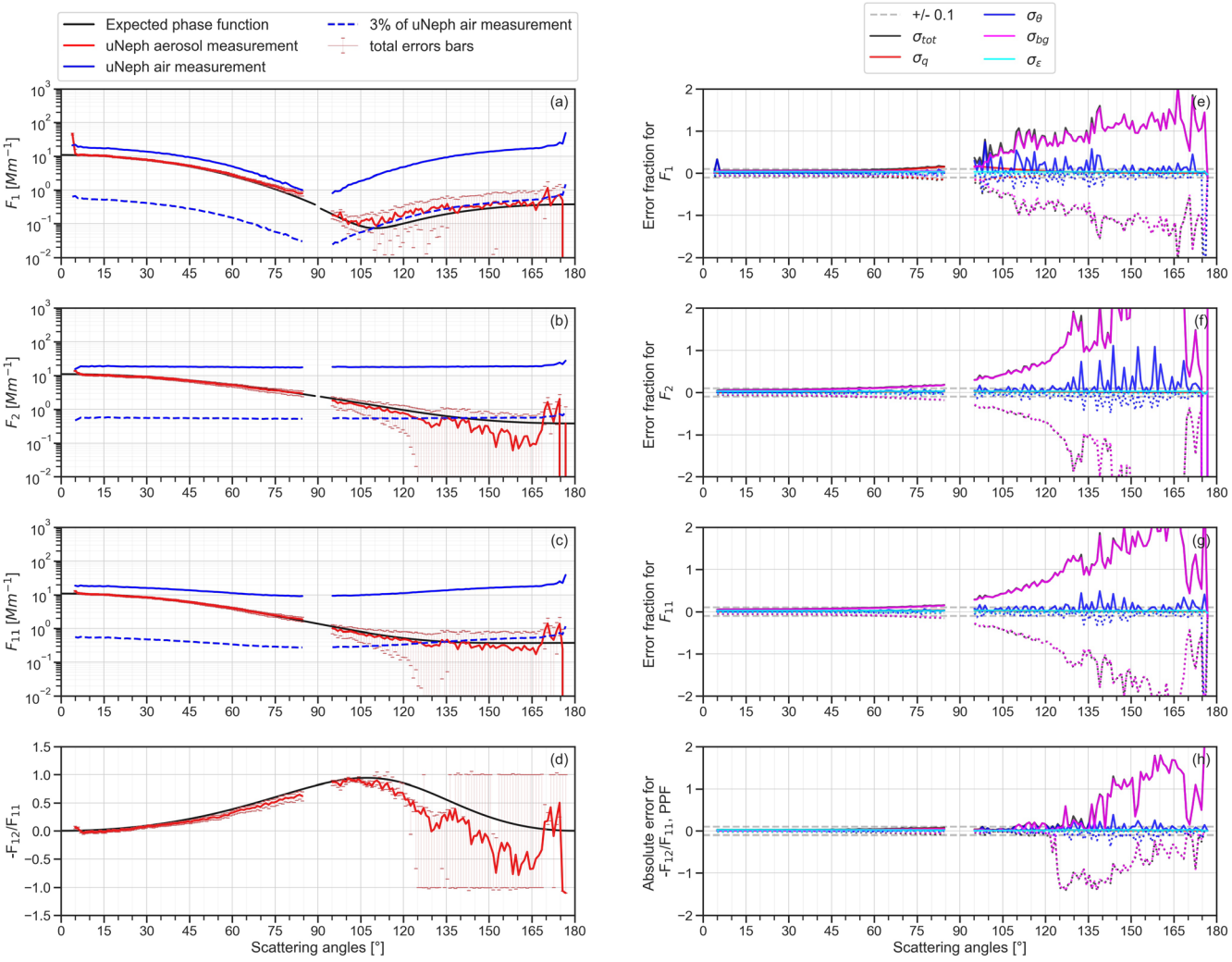


**Figure S20. (a, b, c, d) angular light scattering measurements with total errors for 250 nm (AAC aerodynamic set point) DEHS aerosol particles at low concentration (70 #/cc). (e, f, g,) relative contributions of considered error factors for $F_1$, $F_2$, and $F_{11}$. (h) Absolute contributions of considered error factors for $-F_{12}/F_{11}$.**

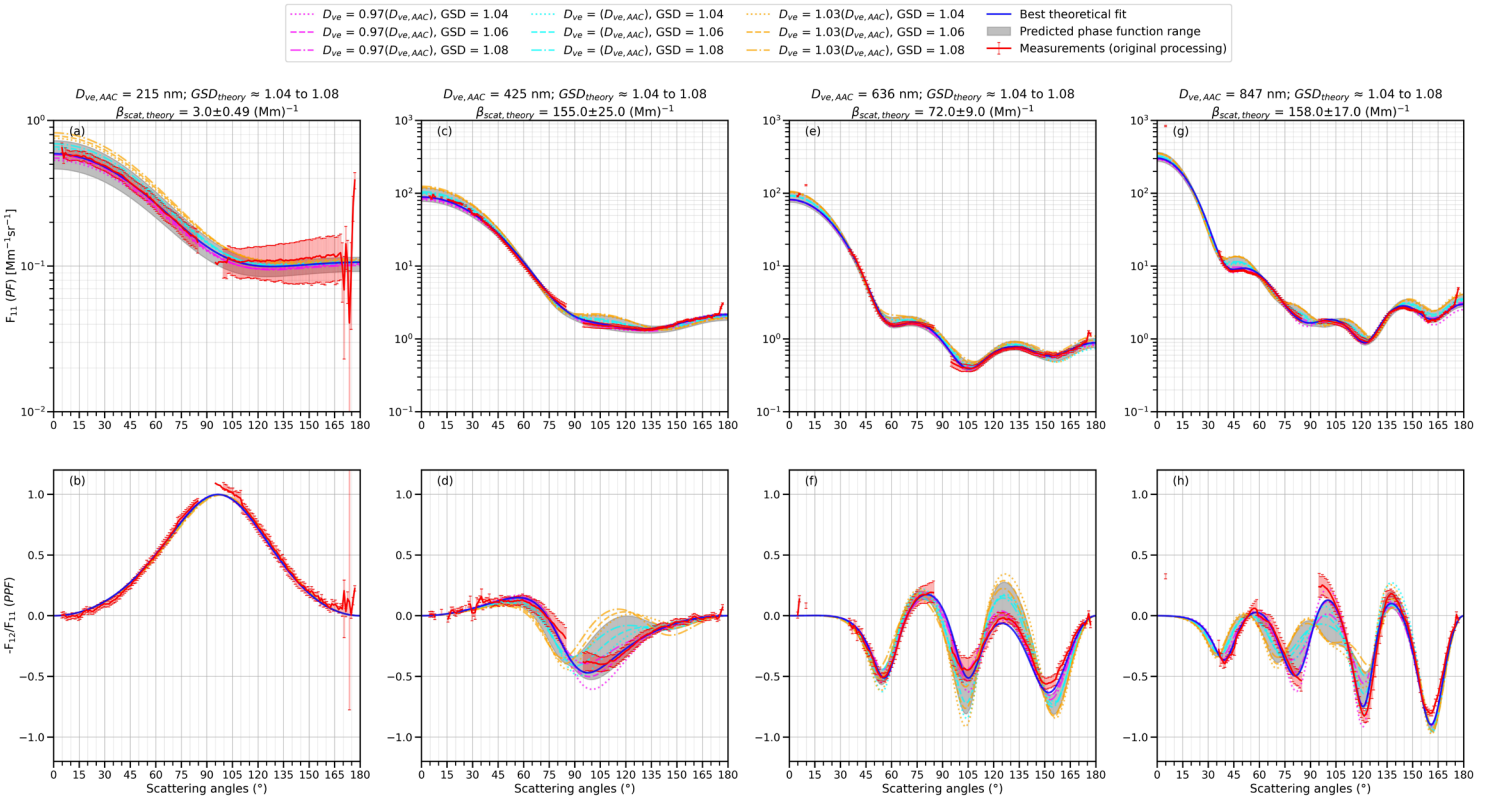


**Figure S21. Same as Fig. 8 but for additional Mie curves for each test cases. The additional Mie curve were simulated at three different $d_m$ corresponding to the AAC set point, $D_{ve}$, AAC (cyan lines), and 0.97 $D_{ve}$, AAC (magenta lines) and 1.03 $D_{ve}$, AAC (yellow lines) which are respectively the high and low extremes of $D_{ve}$, AAC within the assumed error range of 3%. Mie curve at each median size case were simulated for three different GSD cases of 1.04, 1.06 and 1.08 (demonstrated at different line styles) and cover the extremes and mid values within the expected variation range of the GSD. The shape of the measurement data is consistent with at least one of the magenta lines, which all represent slightly smaller diameter than AAC set point while differing in underlying GSD. By contrast, discrepancies between measurement data and all cyan or yellow lines go beyond estimated measurement uncertainty. These findings support the conclusion that measured phase functions are self-consistent across different angles and that they tightly constrain the retrieved diameter. The small but systematic low bias of retrieved diameters compared to AAC set points could just as plausibly be attributed to a small bias of the AAC.**